Energy & Environmental Science

ROYAL SOCIETY OF CHEMISTRY

PAPER

View Article Online
View Journal | View Issue

Cite this: *Energy Environ. Sci.*, 2025, **18**, 4800

A dynamic cathode interlayer for ultralow self-discharge and high iodide utilization in zinc–iodine batteries†

Junming Kang,‡[a] Jiajia Zhang,‡[a] Wang Wan,[b] Zhimin Zhai,[a] Ganxiong Liu,[b] Ying Ge,[a] Lequan Wang,[a] Chao Wang *[b] and Hongbin Lu *[ac]

Received 26th November 2024,
Accepted 8th April 2025

DOI: 10.1039/d4ee05584e

rsc.li/ees

Aqueous zinc–iodine ($Zn–I_2$) batteries are highly desirable for grid energy storage but are subjected to polyiodide shuttling, which leads to low coulombic efficiency (less than 98%), severe self-discharge (over 10% after 2 days) and low iodine utilization (below 80%). In this study, we *in situ* constructed a dynamic interlayer on the cathode surface using an electrolyte additive that can rapidly react with polyiodides. This interlayer effectively prevents polyiodide dissolution and migration in the electrolyte, achieving a high coulombic efficiency of 99.8% at 0.2 A g^{-1} and an ultralow self-discharge rate of 2.9% after 7 days of resting. Remarkably, the interlayer also exhibits good electrochemical activity during cycling. The reacted polyiodides can be reduced to I^- ions during discharge, contributing to the cell capacity and improving the iodine utilization rate to 89.1% at a high capacity of 2.9 mAh cm^{-2}. Moreover, the additive greatly enhances zinc plating behavior, resulting in an extended cycle life of over 36 000 without capacity decay at 5.0 A g^{-1}. At a high mass loading of 15 mg cm^{-2} and a low N/P ratio of 1.85, the battery shows 100% capacity retention after 330 cycles with an impressive energy density of 98 W h kg^{-1}.

Broader context

Aqueous zinc–iodine batteries are a promising form of energy storage technology due to their inherent advantages of low cost, high safety, abundant resources, and fast redox chemistry. Nevertheless, their development is hindered by the shuttle effect of polyiodides, which leads to severe capacity loss and self-discharge. An effective strategy to suppress polyiodide shuttling is to design functional interlayers between the cathode and electrolyte. However, these artificial interlayers are typically electrochemically inactive and involve a complex manufacturing process. Herein, we demonstrate the *in situ* formation of a cathode interlayer through the reaction between an electrolyte additive and polyiodides during charging. This process prevents polyiodide dissolution and migration, significantly addressing issues such as low coulombic efficiency, severe self-discharge, and zinc corrosion caused by the shuttle effect. Additionally, the cathode interlayer is electrochemically active, allowing polyiodides to participate in redox reactions during discharging, which enhances the cell capacity and improves iodine utilization. This work offers valuable insights into the advancement of shuttle-free iodine-based batteries.

Introduction

The development of energy storage systems featuring inherent safety, affordable cost, and environmental benignity has emerged as a global focus.[1] Aqueous $Zn–I_2$ batteries are notable for their non-combustible nature, abundant resources, fast redox kinetics, and great cycle stability, and are expected to be promising candidates for advanced energy storage technologies.[2,3] Nevertheless, $Zn–I_2$ batteries generally suffer from the notorious shuttle effect of polyiodide intermediates (*e.g.*, I_3^-, I_5^-).[4] These polyiodides tend to dissolve into the aqueous electrolyte, leading to a loss of active iodine species, which in turn reduces the coulombic efficiency (CE) and iodine utilization.[5] Additionally, the dissolved polyiodides will diffuse toward the anode and react with the zinc metal. The "anode" and "cathode" refer to the zinc electrode and iodine electrode in the discharge state, respectively. This not only causes zinc corrosion but also leads to severe self-discharge, considering the electron transfer bypassing the external circuit.[6,7] To address these issues, tremendous efforts have been put into investigations including suppressing polyiodide dissolution

[a] *State Key Laboratory of Molecular Engineering of Polymers, Department of Macromolecular Science, Fudan University, Shanghai, 200438, China. E-mail: hongbinlu@fudan.edu.cn*
[b] *School of Materials Science and Engineering, Tongji University, Shanghai, 201804, China. E-mail: chaow@tongji.edu.cn*
[c] *Yiwu Research Institute of Fudan University, Yiwu, 322000, Zhejiang, China*

† Electronic supplementary information (ESI) available. See DOI: https://doi.org/10.1039/d4ee05584e

‡ These authors contributed equally to this work.

with cathode hosts,[8,9] impeding polyiodide corrosion by anode coating,[10,11] blocking polyiodide diffusion *via* separator modification,[12,13] and decreasing polyiodide concentration through electrolyte regulation.[14,15]

Among these approaches, using electrolyte additives is considered a facile and cost-effective strategy to mitigate the adverse shuttle effect and zinc corrosion simultaneously.[16,17] These additives can be categorized into two groups: one inhibits the generation of polyiodides, and the other prevents polyiodide migration. The former are able to deactivate the reaction between I_2 and I^- ions by preferentially coordinating with I_2[14] or altering the solvation structure of I^- ions.[18] The latter could immobilize I_3^- ions by anchoring them in the catholyte[19] or transforming them into gelatinous precipitates.[20] Benefiting from the suppression effect of additives, the coulombic efficiency and cycle life of Zn–I_2 batteries have been significantly improved. Nonetheless, the practical application of Zn–I_2 batteries is still challenged by the undesirable self-discharge rate (over 10% after 48 hours of storage at full charge state) and iodine utilization rate (below 80% at high areal capacity).

An alternative tactic to suppress the shuttle effect is constructing functional interlayers between the cathode and electrolyte.[21] These interlayers can prevent polyiodides from dissolving into the electrolyte and diffusing toward the anode by chemically adsorbing or repelling them through coulombic forces.[22] As a result, the problems caused by the shuttle effect can be effectively resolved. However, this achievement is at the expense of increased cost, considering the expensive raw materials or tedious manufacturing process involved in artificial interlayers.[23] In addition, these artificial interlayers are electrochemically inactive, which inevitably adds to the weight of inactive components, thus negatively impacting the practical specific capacity and energy density.[24,25]

In this work, we developed a dynamic cathode interlayer for aqueous Zn–I_2 cells through a tetramethylammonium iodide (TMAI) electrolyte additive. As illustrated in Fig. 1, tetramethylammonium cations (TMA^+) react with polyiodides during charging to form an *in situ* interlayer on the cathode surface. This interlayer effectively suppresses polyiodide dissolution and diffusion, resulting in high coulombic efficiency and ultralow self-discharge. The battery shows an average CE of 99.8% at 0.2 A g^{-1}, and the self-discharge rate is just 2.9% after resting for 7 days in the fully charged state. Additionally, the interlayer is electrochemically active and can be reduced during discharging, converting polyiodides back into I^- ions. This allows the interlayer to reversibly dissolve and reform, boosting the overall capacity and enabling high iodine utilization. Moreover, the addition of TMA^+ ions improves zinc plating behavior, significantly inhibiting zinc dendrites and enhancing cycling performance. The Zn–I_2 battery demonstrates an ultralong cycle life of over 36 000 cycles at 5 A g^{-1} without capacity decay. We further evaluated the electrochemical performance of the cell with a low N/P ratio of 1.85, which exhibits stable cycling for over 330 cycles and delivers a high energy density of 98 W h kg^{-1} (based on the active materials in both electrodes). The pouch cell also achieves an impressive capacity retention of 91.3% after 100 cycles at a current density of 1 mA cm^{-2}, with exceptional iodine utilization of 89.1% (based on the iodine in both the cathode and electrolyte).

Results and discussion

Electrochemical properties improved by TMAI

Quaternary ammonium compounds can coordinate with polyiodides through Lewis acid–base interactions, making them promising captors of dissolved polyiodides.[26,27] As the simplest

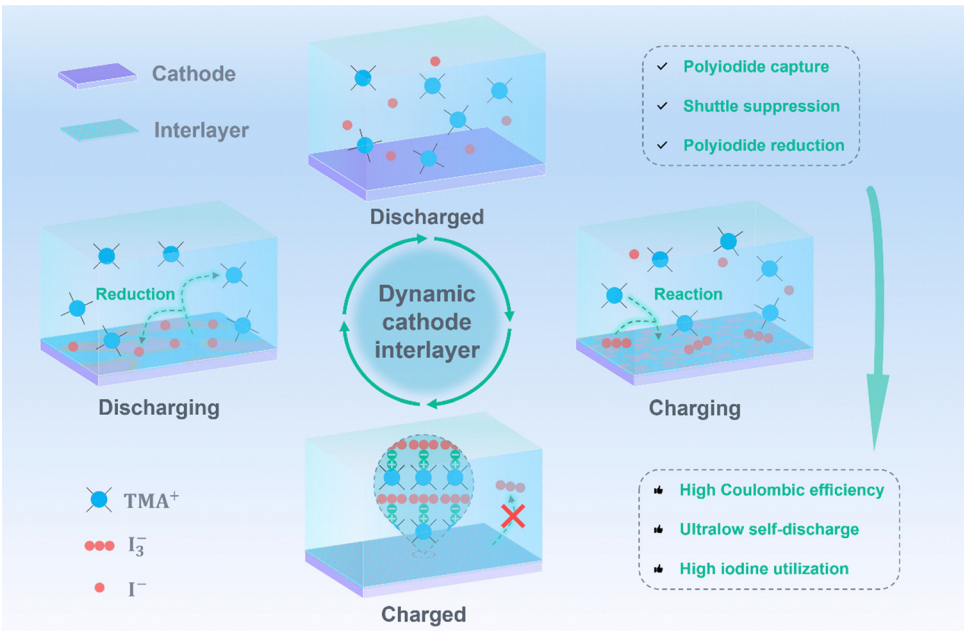

Fig. 1 Schematic of the evolution of the dynamic cathode interlayer in the Zn–I_2 battery.

quaternary ammonium iodide, TMAI occupies the minimum inactive mass, thereby identified as the prototypical electrolyte additive. Quantum chemical calculations were firstly performed to evaluate the interaction between TMAI and iodine species. The molecular electrostatic potential (MESP) of the TMA^+ cation in Fig. 2a illustrates that the nitrogen atom has the most positive MESP value, making it prone to absorb negatively charged polyiodides anions. Fig. 2b exhibits the calculated complexes between TMA^+ and three iodine species, with the corresponding binding energies (E_b) presented in Fig. 2c. The negative E_b values of the three complexes indicate the great absorption competence of TMAI. Notably, the E_b values of I_3^- and I_5^- ions are much more negative than that of I_2, manifesting that the predominant absorbates are polyiodides rather than iodine.

To determine the optimal concentration of the TMAI additive, we firstly selected a 2 M $ZnSO_4$ aqueous solution as the baseline electrolyte (referred to as BE). Fig. S1 (ESI†) shows the electrolytes with varying amounts of TMAI. Notably, it is beyond the solubility limit after adding 0.2 M TMAI. As presented in Fig. 2d, the discharge capacity and coulombic efficiency at a current density of 0.5 A g^{-1} increase with the addition of TMAI. The initial capacity is 196.9 mA h g^{-1} at 0.1 M TMAI, significantly higher than the 135.1 mA h g^{-1} of the BE electrolyte. Fig. 2e reveals that the 0.1 M TMAI exhibits the highest capacity retention and average CE, reaching 95.3% and 99.9%, respectively.

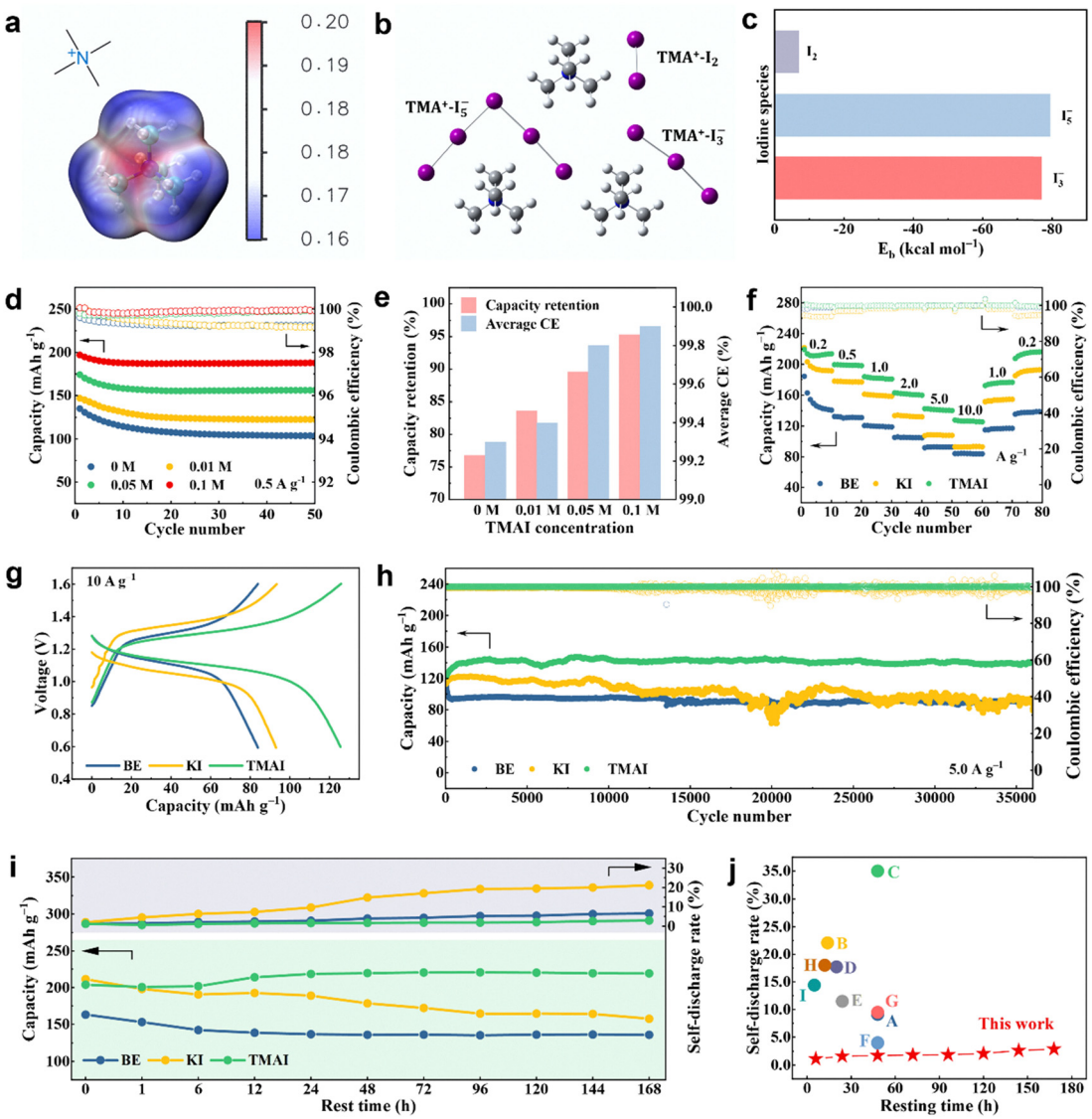

Fig. 2 Electrochemical properties improved by TMAI. (a) Calculated molecular electrostatic potential of TMA^+ ions. (b) and (c) Calculated models and binding energies between the TMA^+ cation and three iodine species. (d) Discharge capacity and coulombic efficiency of batteries containing different amounts of TMAI. (e) Comparison of the capacity retention and average CE for batteries containing different amounts of TMAI. (f) The rate capability of three batteries at different current densities. (g) The GCD curves of the cells with different electrolytes at 10.0 A g^{-1}. (h) The cycle stability of three batteries at 5.0 A g^{-1}. (i) The self-discharge behaviors of Zn–I_2 batteries with different electrolytes. (j) A comparison of the self-discharge rate of this work to other reports. A: ref. 12; B: ref. 18; C: ref. 19; D: ref. 40; E: ref. 41; F: ref. 43; G: ref. 33; H: ref. 44; I: ref. 45.

The impact of TMA^+ cations and I^- anions in the electrolyte was explored through substituting TMAI with tetramethylammonium chloride (TMACl). The electrolyte with TMACl (Fig. S2, ESI†) shows an initial capacity of 189.2 mA h g^{-1} and an average CE of 99.9% at 0.5 A g^{-1}. However, its capacity retention is only 81.8%, which is slightly higher than the 79.2% of the BE electrolyte but lower than the 95.3% of the TMAI electrolyte. These results suggest that TMA^+ enhances the discharge capacity and coulombic efficiency, while the additional I^- primarily improves the capacity retention, though it may also contribute to the overall capacity to some extent.

The electrochemical properties were systematically investigated to evaluate the effect of the TMAI additive. The cathode was prepared by a simple melt diffusion method, and the mass ratio of iodine is 50.2% (Fig. S3, ESI†). Refer to the ESI† for detailed preparation procedures. The cyclic voltammetry (CV) curves collected at different sweep rates are presented in Fig. S4 (ESI†). The TMAI electrolyte shows a pair of redox peaks at all sweep rates, with a slightly increased potential polarization of 134 mV and 82 mV when the sweep rate rises from 1 mV s^{-1} to 10 mV s^{-1}. Similar CV curve profiles are observed in the BE electrolyte, but its peak currents are noticeably smaller than those of TMAI. This implies that the TMAI electrolyte does not change the redox reaction of the Zn–I_2 battery but enhances its electrode reaction kinetics.[19,34] To further clarify the mechanism of charge transfer and redox kinetics, the relationship between peak currents and sweep rates is illustrated in Fig. S5 (ESI†). The peak currents show a linear correlation with the square root of sweep rates, indicating that the redox reaction is predominated by mass diffusion.[18] Fig. S6 (ESI†) depicts the corresponding Zn^{2+} diffusion coefficients calculated using the classic Randles–Sevcik equation based on the slopes of fitted curves.[35,36] It is noteworthy that the values of the TMAI electrolyte reach 1.17×10^{-7} cm s^{-1} and 1.25×10^{-7} cm s^{-1} in the reduction and oxidation process, approximately 2.5 and 2.6 times those of the BE electrolyte, respectively. These enhanced electrode kinetics could be ascribed to that TMA^+ cations have accelerated the charge transfer in the I^0/I^- conversion by stabilizing the soluble polyiodides.[37]

Galvanostatic charge–discharge (GCD) tests were performed to explore the rate capability and cycle stability improved by the TMAI additive. To distinguish the function of I^- ions alone in additive, the electrolyte containing KI was also examined. As revealed in Fig. 2f, the battery with TMAI delivers an initial discharge capacity of 219.5 mA h g^{-1} at 0.2 A g^{-1}, with an exceptional average CE of 99.8%. When the current density increases to 10 A g^{-1} and then returns to 0.2 A g^{-1}, the capacity remains at 128.0 mA h g^{-1} and 216.5 mA h g^{-1}, accounting for 58.3% and 98.6% of the initial capacity, respectively. In stark contrast, the battery with KI electrolyte exhibits an average CE of 93.9% at 0.2 A g^{-1}, implying that the addition of I^- ions without TMA^+ leads to a decrease in coulombic efficiency. As the current density reaches 10 A g^{-1} and then returns to 0.2 A g^{-1}, the capacity retentions are 42.0% and 86.8%, respectively, indicating suboptimal performance in the absence of TMA^+ cations. For the battery with BE electrolyte, it delivers the least capacity at all current densities, with an average CE of 98.7% at 0.2 A g^{-1}, higher than that of the KI electrolyte but lower than TMAI. The corresponding GCD curves are presented in Fig. S7 (ESI†). The cell with TMAI showcases a slight voltage hysteresis of 90 mV when the current density increases from 0.2 A g^{-1} to 10 A g^{-1}. This voltage polarization is significantly lower than those in KI and BE electrolytes, as highlighted in Fig. 2g.

The cycle performance of three batteries is illustrated in Fig. S8 (ESI†) and Fig. 2h. The cell with the TMAI additive shows an initial discharge capacity of 202.0 mA h g^{-1} and a capacity retention of 99.0% after 3600 cycles at 0.5 A g^{-1}, along with an ultrahigh average CE of around 99.9%. As expected, the discharge capacity, capacity retention and coulombic efficiency obtained from its two counterparts are inferior to those of the TMAI electrolyte. In particular, the average CEs of KI and BE electrolytes are 96.0% and 98.2%, respectively, distinctly lower than that of TMAI, conforming to the results from the rate measurements. At a higher current density of 5.0 A g^{-1}, the battery containing TMAI could stably operate for over 36 000 cycles with imperceptible capacity decay. This is markedly different from the performance of those with KI and BE electrolytes, which appear conspicuously fluctuant and decreasing. Compared with pioneering works on Zn–I_2 batteries, the cell with the TMAI additive achieves impressive cycle durability (Fig. S9, ESI†).[28–32,38–43]

The self-discharge behavior, a pivotal indicator of practical application, was assessed by resting fully charged cells for different durations. Fig. 2i depicts the discharge capacity and self-discharge rate of three batteries after resting for different times, with the corresponding discharge curves plotted in Fig. S10 (ESI†). The cell with the BE electrolyte delivers a discharge capacity of 135.6 mA h g^{-1} and a self-discharge rate of 6.57% after resting for 168 h (7 days). Despite a higher discharge capacity of 157.44 mA h g^{-1} (ascribed to a higher charge capacity), the self-discharge rate of the battery with KI increases to 21.3% after 7 days of resting, implying a deteriorative self-discharge phenomenon. In the same circumstance, a superb capacity of 219.2 mA h g^{-1} and an ultralow self-discharge rate of 2.9% are achieved in the cell with TMAI. The comparison of the self-discharge rate from this work with other reports is shown in Fig. 2j, which highlights the best anti-self-discharge performance to date.[12,18,19,33,40,41,43–45] In brief, the superior electrochemical properties demonstrate that the addition of TMAI has simultaneously improved the overall capacity, coulombic efficiency, capacity retention, and anti-self-discharge.

Suppression of the polyiodide shuttle effect

The low coulombic efficiency and self-discharge behavior of Zn–I_2 batteries are ascribed to the shuttle effect of polyiodide intermediates. To explicitly unravel the shuttle effect, we collected *in situ* optical photographs (Fig. 3a) of the three electrolytes at different voltages (Fig. 3b). A noticeable yellow color in the BE electrolyte appears at 1.4 V and intensifies at 1.6 V, implying the appearance and accumulation of polyiodides. In the following discharge process, the yellow color gradually fades but spreads to the adjacent solution, attributed to the

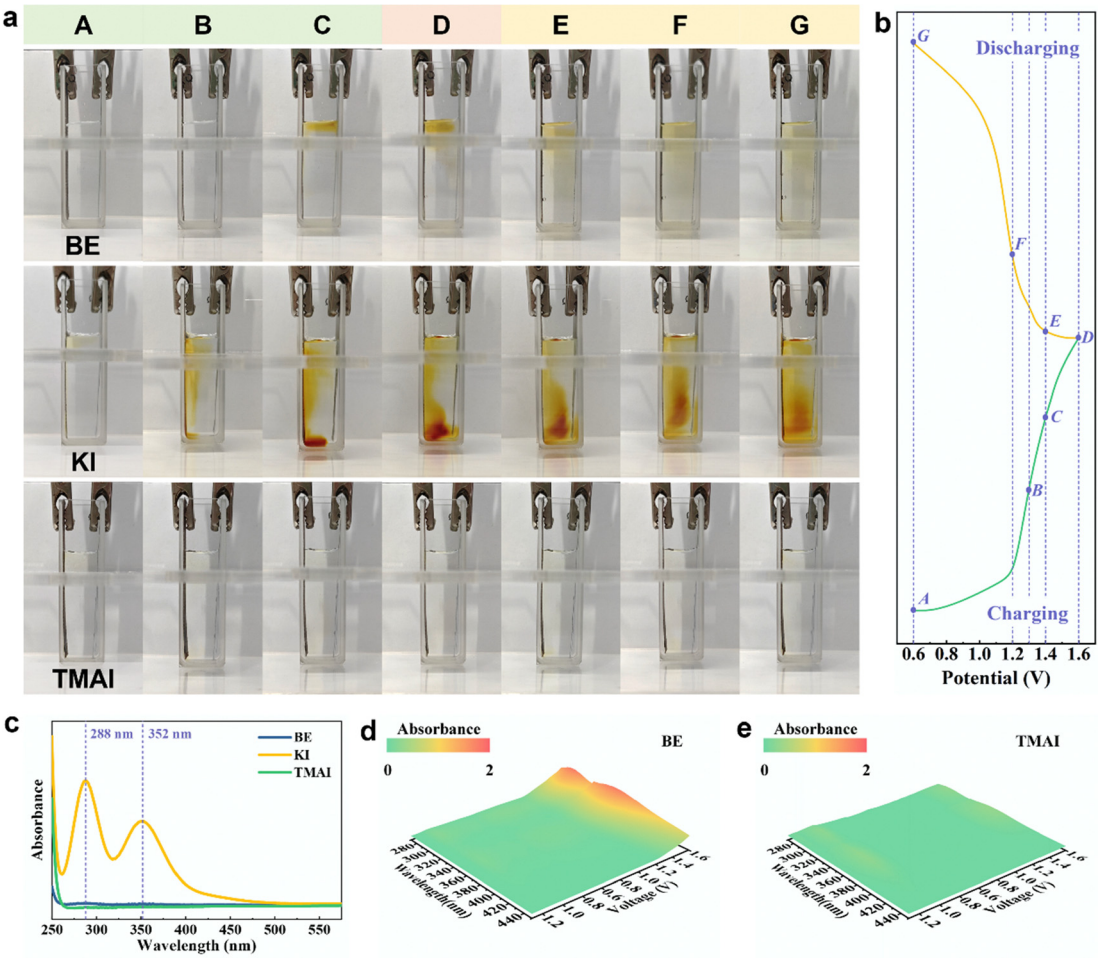

Fig. 3 Suppression of the polyiodide shuttle effect. (a) *In situ* optical photographs of the shuttle effect in different batteries. (b) Corresponding GCD curves with marked voltage points. (c) UV-vis spectra of different electrolytes after *in situ* optical experiments. (d) and (e) *In situ* UV-vis spectra of BE and TMAI electrolytes.

diffusion of polyiodides driven by a concentration gradient. The electrolyte with KI exhibits a more rapid and pronounced color change, which clearly discloses the aggravated dissolution and diffusion of polyiodides in the absence of TMA^+. As expected, there is no discernable color change in the TMAI electrolyte throughout the charge/discharge process, corroborating the significantly suppressed shuttle effect. The ultraviolet-visible (UV-vis) spectra of three solutions after being fully discharged, shown in Fig. 3c, further verify that TMAI effectively mitigates the dissolution of polyiodides, considering the undetectable characteristic peaks of I_3^- ions in the TMAI electrolyte.

In situ UV-vis spectroscopy was employed to monitor the evolution of polyiodides in different electrolytes. In Fig. 3d, the increasingly prominent UV-vis absorbance of I_3^- ions suggests polyiodide dissolution into the BE electrolyte during the charge stage. For the KI electrolyte (Fig. S11, ESI†), the absorption peaks of I_3^- emerge during the initial discharge stage and fade away as the voltage decreases. But these peaks then reappear with heightened intensity during the following charge process, which signifies the deteriorative shuttle effect. Intriguingly, the TMAI electrolyte exhibits neglectable UV-vis signals throughout the process, as depicted in Fig. 3e, demonstrating that the shuttle effect has been effectively mitigated. The pivotal role of TMA^+ cations in suppressing the dissolution and diffusion of polyiodides is further illustrated in Fig. S12 (ESI†). Having immersed the cathode into the electrolyte containing KI, we observed an increasingly yellowing solution over the resting period. In contrast, the electrolyte containing TMAI remains constantly transparent, with minimal color change even after 10 days of resting. The UV-vis spectra of the two final solutions are presented in Fig. S13 (ESI†), where the absorption peaks of I_3^- ions in the KI electrolyte are notably higher than those of TMAI. This indicates the impeded dissolution of polyiodides facilitated by the TMAI additive.

Characterization of the dynamic cathode interlayer

To gain insights into the intrinsic mechanism of TMAI in suppressing the polyiodide shuttle effect, we recorded the *in situ* morphology evolution of the cathode surface in a customized electrolytic cell (Fig. S14, ESI†). The optical photographs and the corresponding GCD curves with marked voltage

points are presented in Fig. 4a. During the charge stage from A to B, the cathode maintains a black color. However, some green substances emerge on the surface at point C and fully cover the cathode at point D. This observation indicates the generation of an interlayer, which remains intact during the following charge stage from D to E. During the subsequent discharge process, despite remaining unchangeable from E to F, this interlayer dissipates at point G and remains absent from H to I. More importantly, this interlayer on the cathode surface forms and disappears reversibly during cycling, as illustrated in Fig. S15 (ESI†).

Ex situ Raman, FTIR, and XRD measurements were performed to identify the components of the interlayer. As depicted in Fig. 4b, the curves at fully discharged stages (Point A and Point I) are identical, showing only noticeable Raman signals of the carbon substrate. However, at the fully charged stage (Point E), the peaks at 109 cm^{-1} and 156 cm^{-1} of polyiodide anions emerge in the Raman spectrum. The FTIR spectra, shown in Fig. 4c, display distinguishable peaks of TMA^+ cations at Point E. The peaks shaded in purple (1483 cm^{-1} and 1402 cm^{-1}) and brown (1292 cm^{-1}) are attributed to the deformation and rocking of methyl groups, while the peaks in cyan (943 cm^{-1}) are ascribed to the skeletal vibration of TMA^+.[46] These results demonstrate the formation of the interlayer, which stems from the reaction between polyiodides and TMA^+ ions. Fig. 4d plots the XRD patterns, where the prominent diffraction peaks (12.50°, 21.47°, and 24.93°) at Point E can be assigned to the crystalline reaction products. Overall, the TMAI additive can react with the dissolved polyiodides to form a dynamic interlayer on the cathode surface. This interlayer helps inhibit the shuttle effect and convert polyiodide intermediates back into I^- ions in Zn–I_2 batteries.

For a better understanding of the formation mechanism of this interlayer, we carried out a visual experiment to explore the reaction between TMA^+ ions and polyiodides. As presented in Fig. 4e, the bright-red solution containing I_3^- ions turns light-yellow after reaction, with some solid precipitates settling at the

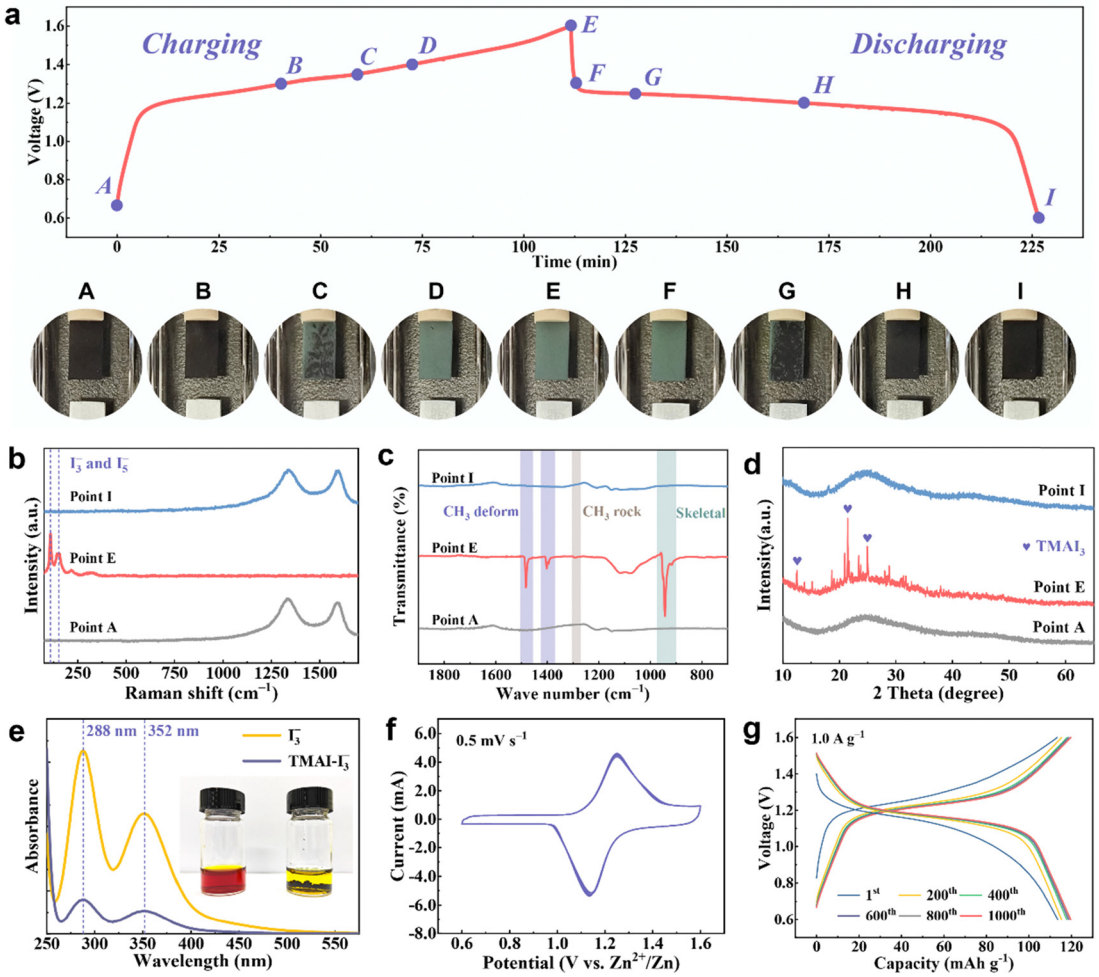

Fig. 4 Characterization of the dynamic cathode interlayer. (a) *In situ* optical photographs of the cathode interlayer and the corresponding GCD curves with marked voltage points. (b)–(d) *Ex situ* Raman, FTIR, and XRD results of the cathode interface. (e) UV-vis spectra and optical photograph of polyiodide solutions before and after the addition of TMAI. The concentrations of I_3^- and TMA^+ are 0.01 M and 0.1 M, respectively. (f) and (g) CV curves and GCD curves of the reaction products at 0.5 mV s^{-1} and 1.0 A g^{-1}.

bottom. The corresponding UV-vis absorbance at 288 nm and 352 nm of the two solutions reveals that this reaction leads to a sharp decline in the concentration of I_3^- ions. We further characterized the morphology and chemical structure of the precipitates. Fig. S16 (ESI†) shows that TMAI morphology presents as large flakes, while the precipitates transform into loose particles with a homogeneous distribution of iodine elements (Fig. S17, ESI†). In the Raman spectra (Fig. S18, ESI†), different from the spectrum of TMAI, the precipitates exhibit a remarkable peak at 108 cm^{-1}, attributed to I_3^- ions. For the FTIR spectra in Fig. S19 (ESI†), the absorption peaks of methyl and skeletal of TMA^+ are observed in both TMAI and precipitates, conforming to the results of the dynamic interlayer. The XRD patterns of TMAI in Fig. S20 (ESI†) align well with JCPDF no. 73-7566 (Fig. S21, ESI†). In contrast, the prominent diffraction peaks of the precipitates at angles of 12.52, 18.72, and 21.52 match well with JCPDF no. 37-1876 (Fig. S21, ESI†), which belongs to tetrabutylammonium triiodide ($TMAI_3$). Additionally, these peaks are consistent with those of the cathode interlayer (Fig. S22, ESI†), implying that the predominant component in the interlayer is $TMAI_3$.

To verify the redox activity of this interlayer, the electrochemical properties of the precipitates were investigated exclusively. As shown in Fig. 4f, the CV curves at 0.5 mV s^{-1} exhibit a pair of redox peaks at 1.25/1.14 V and remain uniform over the following three cycles. The GCD curves at 1.0 A g^{-1} display a distinct charge/discharge plateau at 1.24/1.17 V (Fig. 4g), with an average CE of 99.9% and capacity retention of over 100% after 1000 cycles (Fig. S23, ESI†). These results reflect that the interlayer possesses excellent redox kinetics and electrochemical reversibility.

Electrochemical stability of zinc anodes

Quaternary ammonium cations have the potential to induce uniform zinc deposition and improve the electrochemical stability of zinc anodes.[47] To elucidate the impact of TMAI on the reversibility of the zinc anode, we examined the coulombic efficiencies of Zn‖Cu asymmetric cells at a current density of 1 mA cm^{-2} and an areal capacity of 1 mA h cm^{-2} (Fig. 5a). The batteries with TMAI and KI electrolytes operate steadily for over 1000 and 968 hours, respectively, with average CEs of 99.6% and 99.5%. For the cell with BE electrolyte, it delivers an average CE of 97.0% and short-circuits after 236 hours. This indicates that the addition of TMAI promotes the reversible zinc plating/stripping behavior.[48] Fig. 5b presents the rate performance of Zn‖Zn symmetric cells at current densities ranging from 0.5 mA cm^{-2} to 20 mA cm^{-2} with an areal capacity of 1 mA h cm^{-2}. The cell with KI electrolyte exhibits

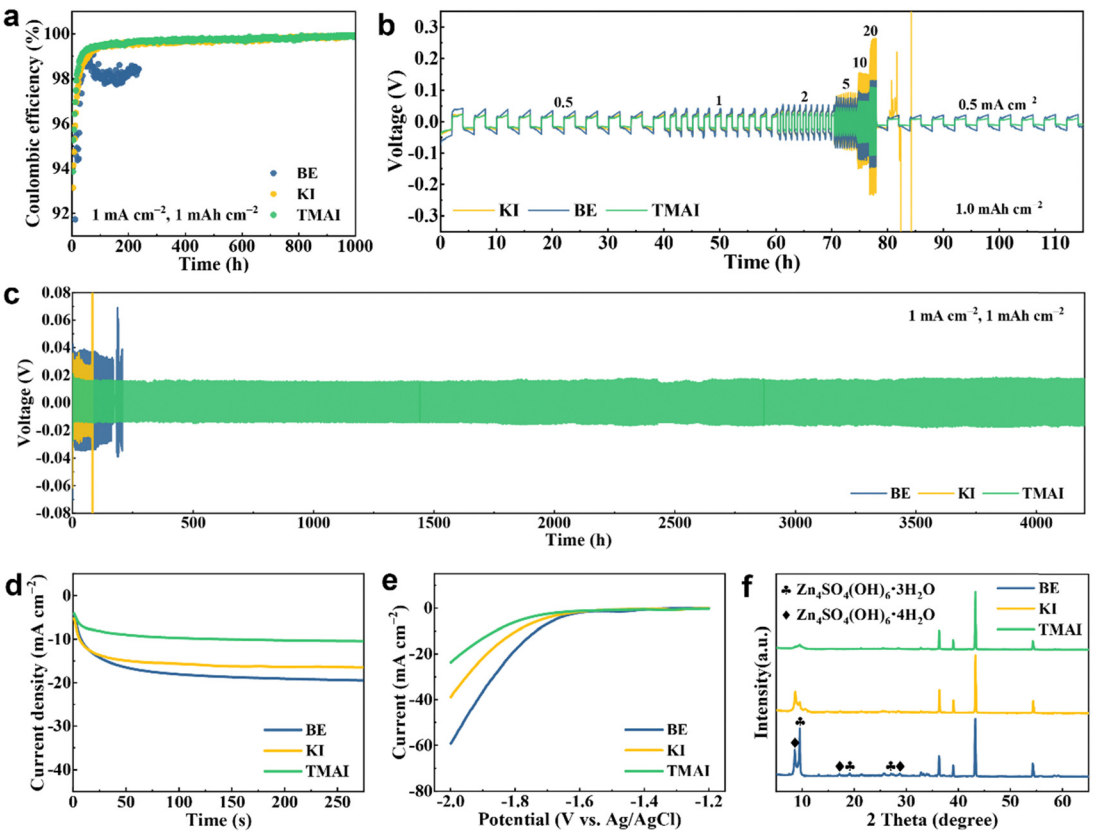

Fig. 5 Electrochemical stability of zinc anodes. (a) Coulombic efficiency of Zn‖Cu asymmetric cells. (b) Rate capability of Zn‖Zn symmetric cells. (c) Cycle stability of Zn‖Zn symmetric cells. (d) CA curves of zinc electrodes in three electrolytes. (e) Hydrogen evolution overpotentials in three electrolytes, where $ZnSO_4$ was replaced by Na_2SO_4 to avoid the interference from the faradaic current of Zn^{2+}. (f) XRD patterns of zinc anodes after immersion in different electrolytes for 7 days.

similar voltage profiles to those with TMAI electrolyte at 0.5 mA cm^{-2}. However, it shows the largest voltage hysteresis as the current density exceeds 2 mA cm^{-2}, and suddenly short-circuits when the current density returns to 0.5 mA cm^{-2}. Intriguingly, the steadiest voltage profiles and smallest voltage polarization are achieved in the TMAI electrolyte at all current densities, highlighting the essential role of TMA^+ cations in improving the deposition behavior of the zinc anode.

To further confirm the significance of the TMAI additive, the long-term cycle performance of Zn‖Zn symmetric cells is depicted in Fig. 5c. At a current density of 1 mA cm^{-2} and an areal capacity of 1 mA h cm^{-2}, the battery with TMAI electrolyte demonstrates an ultralong cycle life of over 4200 h, with a slight voltage polarization of less than 180 mV. In contrast, the batteries with KI and BE electrolytes cycle steadily for only 80 h and 160 h, respectively, with larger voltage polarizations of more than 270 mV and 310 mV. This observation aligns with the smallest charge transfer impedance in the TMAI electrolyte, as plotted in Fig. S24 (ESI†). The battery containing TMAI also showcases a lifespan of over 1000 h at a higher current density and areal capacity (5 mA cm^{-2}, 5 mA h cm^{-2}), much longer than those of its counterparts without TMA^+ ions (Fig. S25, ESI†). The SEM images of different zinc anodes in Fig. S26 (ESI†) could account for the superior cycle stability improved by TMAI. Unlike the loosened petal-shaped dendrites in the BE electrolyte and the blade-shaped morphology in the KI electrolyte, a uniform and compact zinc deposition is achieved in the TMAI electrolyte.

We conducted chronoamperometry (CA) tests to investigate the effect of TMAI on zinc deposition behavior. It is well known that the current in CA tests directly reflects the deposition morphology of Zn^{2+} ions.[49,50] An increase in current indicates a rise in the true surface area of the zinc electrode during deposition. As shown in Fig. 5d, all three curves exhibit a rapid increase in current within the first 8 seconds, corresponding to the Zn^{2+} nucleation process. As the deposition continues, the BE and KI electrolytes exhibit a significant increase in current density, indicating a prominent increase in the true surface area of zinc electrodes. This is primarily due to the 2D diffusion of Zn^{2+} and the formation of Zn dendrites, which lead to a loose and rough electrode morphology, as evidenced in Fig. S26 (ESI†). In contrast, in the TMAI electrolyte, the current density increases slightly and stabilizes within 60 seconds, suggesting suppressed 2D diffusion of Zn^{2+} and reduced Zn dendrite growth. This optimization can be attributed to the electrostatic shielding effect of the TMA^+ ions. Specifically, the adsorbed TMA^+ ions on the zinc electrode prevent Zn^{2+} from laterally diffusing and aggregating into dendrites, resulting in a uniform and compact zinc deposition morphology (Fig. S26, ESI†). The linear sweep voltammetry (LSV) curves in Fig. 5e indicate that the TMAI electrolyte shows the lowest hydrogen evolution overpotential of –1.70 V *vs.* Ag/AgCl, demonstrating an effectively inhibited hydrogen evolution due to the addition of TMA^+ ions.[51] Fig. 5f depicts the XRD patterns of zinc anodes immersed in different electrolytes for 7 days. Notably, two distinct diffraction peaks at 8.58° and 9.54° are observed in BE and KI electrolytes. These peaks are assigned to the corrosion products $Zn_4SO_4(OH)_6{\cdot}4H_2O$ and $Zn_4SO_4(OH)_6{\cdot}3H_2O$, considering their accordance with JCPDF no. 44-0673 and JCPDF no. 44-0673 (Fig. S27, ESI†). In contrast, the TMAI electrolyte shows only a weak peak at 9.52°, which corroborates that TMAI significantly impedes the zinc corrosion.

The anti-corrosion effect of TMAI was also estimated in Zn–I_2 full cells. The anodic morphology after 50 cycles at 5 A g^{-1} (Fig. S28, ESI†) reveals a smoother and denser zinc deposition in the TMAI electrolyte, benefitting from the shielding effect of TMA^+ ions. The corresponding XRD patterns are presented in Fig. S29 (ESI†). They indicate that the peaks of by-products, including $Zn_4SO_4(OH)_6{\cdot}5H_2O$, $Zn_4SO_4(OH)_6{\cdot}3H_2O$, and $Zn(OH)_2{\cdot}0.5H_2O$ (with JCPDF cards in Fig. S30, ESI†), are detectable in BE and KI electrolytes. However, these peaks are absent in the TMAI electrolyte, further confirming the good efficacy of TMAI in resisting zinc corrosion. In brief, the TMAI additive in electrolyte is effective in suppressing zinc dendrites and the correlative side reactions due to the shielding effect of TMA^+ cations.

To clarify the regulatory mechanism of TMAI for improving the stability of zinc anodes, we investigated the adsorption behavior of I^- and TMA^+ ions on zinc surfaces. Density functional theory (DFT) calculations were employed to explore the adsorption energies (E_{ads}) of H_2O, I^- and TMA^+ on Zn (001) crystal planes, with the adsorption models illustrated in Fig. S31 (ESI†). As shown in Fig. S32 (ESI†), both I^- and TMA^+ ions exhibit much lower E_{ads} values compared to water molecules, suggesting that they are prone to adsorb on the zinc surfaces.[52,53] Notably, the most negative E_{ads} for TMA^+ implies its strongest adsorption capability, which will be discussed further below. The electric double layer (EDL) capacitances in different electrolytes were examined through the CV tests of Zn‖Zn symmetric cells. For eliminating the interference from the faradaic current of Zn^{2+}, we substituted $ZnSO_4$ with Na_2SO_4. Fig. S33 (ESI†) depicts the CV curves at various sweep rates, and we obtained the EDL capacitances according to previous reports.[54,55] Specifically, capacitance values were calculated based on the equation of $C = i/\nu$, where C is the capacitance and ν is the sweep rate, and i is half the current difference between the positive and negative sweeps. As shown in Fig. S34 (ESI†), the BE electrolyte exhibits an EDL capacitance of 2.18 mF cm^{-2}, which is lower than the 2.25 mF cm^{-2} of KI but higher than the 1.73 mF cm^{-2} of TMAI. The increased EDL capacitance in the KI electrolyte can be attributed to the adsorbed I^- ions on the zinc surface, which promotes the aggregation of Zn^{2+} and results in a reduced thickness of diffusion layer. As for the TMAI electrolyte, both I^- and TMA^+ ions could adsorb on the zinc surface. But compared to I^- ions, the stronger adsorption capability of TMA^+ contributes to its higher adsorption amount. The adsorbed TMA^+ ions increase the thickness of the diffusion layer and, consequently, reduce the EDL capacitance in TMAI.

Alternating current voltammetry was used to measure the differential capacitances (C_s) in three electrolytes containing Na_2SO_4.[52,55] Fig. S35 (ESI†) manifests that the C_s values for the KI electrolyte are higher than those of the BE electrolyte in the

potential range from −1.5 V to −1.0 V. In contrast, the TMAI electrolyte displays lower C_s values compared to the BE electrolyte. These results agree with the EDL capacitance data, confirming the preferential adsorption of TMA^+ and I^- ions on zinc surfaces. Additionally, we conducted zeta potential tests on zinc metal in the electrolyte solutions, which are collected by ultrasonically treating the deposited zinc (1 mA cm^{-2} and 1 mA h cm^{-2}) from titanium foils into the three electrolytes. As presented in Fig. S36 (ESI†), the zeta potentials in KI and TMAI electrolytes are higher and lower, respectively, than that in the BE electrolyte, further verifying the adsorption behaviors of TMA^+ and I^- ions on the surface of zinc anodes.[50,55] Based on these results, the mechanism that TMAI regulates the Zn^{2+} deposition can be summarized as follows. On the one hand, the preferential adsorption of TMA^+ and I^- ions reduce the number of active water molecules on the zinc surface, contributing to a EDL structure with limited water.[56] This H_2O-poor EDL near the Zn anode helps suppress water-induced side reactions, such as the hydrogen evolution reaction and the formation of zinc corrosion by-products. On the other hand, the adsorbed TMA^+ on zinc surfaces could repulse Zn^{2+} ions, preventing them from laterally diffusing and gradually aggregating to form dendrites.[47,49]

Practical application of Zn–I_2 full cells

Based on the bifunctional effect of the TMAI additive on both electrodes, we estimated its feasibility under more rigorous conditions and in pouch-type cells. As shown in Fig. 6a, a cycle life of over 330 cycles is achieved in the TMAI battery with a low N/P ratio of 1.85 at a current density of 5 mA cm^{-2}, together with a maximum discharge capacity of 2.2 mA h cm^{-2} and an average CE of 99.9%. Correspondingly, the energy density of this battery reaches 98 W h kg^{-1} based on the active materials in both the cathode and anode. In stark contrast, the battery with the BE electrolyte exhibits dramatic capacity decay after 90 cycles, accompanied by severe fluctuations in coulombic efficiency. The corresponding GCD curves of two batteries, plotted in Fig. S37 (ESI†), reveal a sharp decline in discharge voltages at 200 and 300 cycles in the BE electrolyte. This voltage decline resulting from the depletion of the zinc metal, is unnoticeable in the TMAI electrolyte, implying improved deposition behavior and inhibited side reactions of the zinc anode.

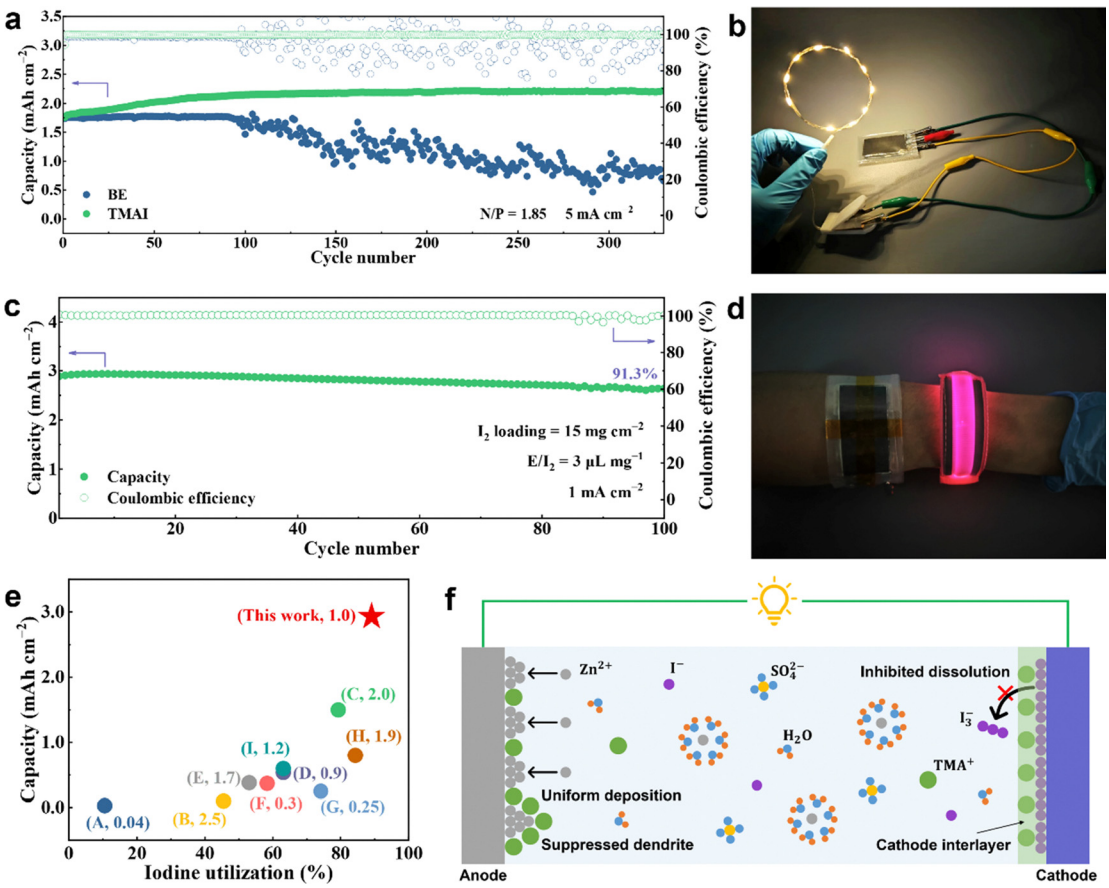

Fig. 6 Practical application of Zn–I_2 full cells. (a) Cycle stability of the batteries with a N/P ratio of 1.85. (b) Optical photograph of the rope light powered by two tandem pouch cells. (c) Cycle durability of the pouch-type cell. (d) Optical photograph of the luminous wristband powered by two tandem pouch cells. (e) Comparison of the areal capacity and iodine utilization of this work to other reports. The references and current densities (mA cm^{-2}) are given in brackets. A: ref. 18; B: ref. 36; C: ref. 38; D: ref. 50; E: ref. 51; F: ref. 52; G: ref. 53; H: ref. 54; I: ref. 55. (f) Schematic of the dual efficacy of TMAI on both electrodes.

Encouragingly, two tandem 2.5 × 4 cm^2 pouch cells with a lean electrolyte (the electrolyte volume/iodine mass ratio, E/I_2 ratio, is controlled around 3) could power a rope light and a luminous wristband (Fig. 6b and d), unraveling the practicality of our Zn–I_2 battery. In addition, a larger 4 × 6 cm^2 pouch cell (Fig. S38, ESI†) showcases an initial discharge capacity of 2.9 mA h cm^{-2} and an impressive capacity retention of 91.3% after 100 cycles at an ultralow current density of 1 mA cm^{-2} (Fig. 6c). Meanwhile, this cell maintains consistent voltage profiles and minimal voltage polarization within 100 cycles (Fig. S39, ESI†), achieving an exceptional iodine utilization of 89.1% based on the iodine in both the cathode and electrolyte. This achievement highlights the superior electrochemical performance of our pouch cell compared to most reports, as evidenced in Fig. 6e.[18,28,38,57–62] Overall, the dual efficacy of the TMAI additive on both electrodes is illustrated in Fig. 6f. During the charge process, a dynamic interlayer forms *in situ* on the cathode surface, due to the reaction between TMA^+ cations and polyiodide intermediates. This interlayer inhibits the dissolution of polyiodides and involves them in the electrode reaction during discharging, thereby impeding the shuttle effect and boosting cell capacity. Additionally, the addition of TMA^+ cations can induce the uniform deposition and prevent the lateral diffusion of zinc ions, significantly mitigating dendritic growth and the associated side reactions.

Conclusion

To summarize, we successfully constructed a dynamic interlayer on the cathode surface of Zn–I_2 cells using TMAI as an electrolyte additive. This interlayer forms *in situ* through the reaction between TMA^+ cations and polyiodide anions during the charging process. By effectively capturing dissolved polyiodides, the interlayer enhances the coulombic efficiency to 99.8% at 0.2 A g^{-1} and reduces the self-discharge rate to 2.9% after 7 days of resting at fully charged state. Notably, as confirmed by *in situ* UV-vis spectroscopy and optical electrochemical experiments, the interlayer actively participates in the redox reactions and fully dissolves during the subsequent discharge process. Acting as an ''extended cathode'', this interlayer not only immobilizes polyiodides but also involves them in electrode reactions, thereby achieving an ultrahigh iodine utilization rate of 89.1% at 2.9 mA h cm^{-2}. Furthermore, TMA^+ ions improve the zinc plating behavior, suppressing the dendrite growth and corrosion reactions. These attributes endow the Zn–I_2 battery with an exceptional lifespan of over 36 000 cycles at 5 A g^{-1} without capacity decay. The remarkable electrochemical performance is also achieved in a low N/P ratio battery and pouch-type cell, which delivers a capacity retention of around 100% after 330 cycles and 91.3% after 100 cycles, respectively. This study indicates that the dynamic cathode interlayer, derived from the reaction of TMA^+ cations and polyiodide anions, is efficient in impeding the shuttle effect, offering prospects for developing long-lifespan, shuttle-free metal–iodine batteries.

Data availability

The data that support the findings of this study are available from the corresponding author upon reasonable request.

Conflicts of interest

There are no conflicts to declare.

Acknowledgements

This work was financially supported by Shaanxi Yanchang Petroleum Co. Ltd (18529), Yiwu Research Institute of Fudan University (21557), the National Natural Science Foundation of China (22075048), and the Shanghai International Collaboration Research Project (19520713900). C. W. acknowledges the support from the Fundamental Research Funds for Central Universities.

References

1 Z. Zhu, T. Jiang, M. Ali, Y. Meng, Y. Jin, Y. Cui and W. Chen, *Chem. Rev.*, 2022, **122**, 16610–16751.
2 H. Chen, X. Li, K. Fang, H. Wang, J. Ning and Y. Hu, *Adv. Energy Mater.*, 2023, **13**, 2302187.
3 L. Zhang, H. Guo, W. Zong, Y. Huang, J. Huang, G. He, T. Liu, J. Hofkens and F. Lai, *Energy Environ. Sci.*, 2023, **16**, 4872–4925.
4 Q. Li, K. K. Abdalla, J. Xiong, Z. Song, Y. Wang, Y. Zhao, M. Liu, Y. Fan, Y. Zhao and X.-M. Sun, *Energy Mater.*, 2024, **4**, 400040.
5 J. Kang, Z. Zhao, H. Li, Y. Meng, B. Hu and H. Lu, *Energy Mater.*, 2022, **2**, 200009.
6 J. Hao, S. Zhang, H. Wu, L. Yuan, K. Davey and S.-Z. Qiao, *Chem. Soc. Rev.*, 2024, **53**, 4312–4332.
7 X. Chen, X. Xie, P. Ruan, S. Liang, W.-Y. Wong and G. Fang, *ACS Energy Lett.*, 2024, **9**, 2037–2056.
8 Y. Tan, Z. Chen, Z. Tao, A. Wang, S. Lai and Y. Yang, *Angew. Chem., Int. Ed.*, 2023, **62**, e202217744.
9 X. Li, N. Li, Z. Huang, Z. Chen, G. Liang, Q. Yang, M. Li, Y. Zhao, L. Ma, B. Dong, Q. Huang, J. Fan and C. Zhi, *Adv. Mater.*, 2021, **33**, 2006897.
10 G. Liang, J. Zhu, B. Yan, Q. Li, A. Chen, Z. Chen, X. Wang, B. Xiong, J. Fan, J. Xu and C. Zhi, *Energy Environ. Sci.*, 2022, **15**, 1086–1096.
11 K. Wang, J.-B. Le, S.-J. Zhang, W.-F. Ren, J.-M. Yuan, T.-T. Su, B.-Y. Chi, C.-Y. Shao and R.-C. Sun, *J. Mater. Chem. A*, 2022, **10**, 4845–4857.
12 Z. Li, X. Wu, X. Yu, S. Zhou, Y. Qiao, H. Zhou and S.-G. Sun, *Nano Lett.*, 2022, **22**, 2538–2546.
13 H. Yang, Y. Qiao, Z. Chang, H. Deng, P. He and H. Zhou, *Adv. Mater.*, 2020, **32**, 2004240.
14 F. Wang, W. Liang, X. Liu, T. Yin, Z. Chen, Z. Yan, F. Li, W. Liu, J. Lu, C. Yang and Q.-H. Yang, *Adv. Energy Mater.*, 2024, **14**, 2400110.
15 Y. Yang, S. Liang, B. Lu and J. Zhou, *Energy Environ. Sci.*, 2022, **15**, 1192–1200.

16 L. Yan, S. Zhang, Q. Kang, X. Meng, Z. Li, T. Liu, T. Ma and Z. Lin, *Energy Storage Mater.*, 2022, **54**, 339–365.
17 D. Lin and Y. Li, *Adv. Mater.*, 2022, **34**, 2108856.
18 T. Xiao, J. Yang, B. Zhang, J. Wu, J. Li, W. Mai and H. J. Fan, *Angew. Chem., Int. Ed.*, 2024, **63**, e202318470.
19 G. Chen, Y. Kang, H. Yang, M. Zhang, J. Yang, Z. Lv, Q. Wu, P. Lin, Y. Yang and J. Zhao, *Adv. Funct. Mater.*, 2023, **33**, 2300656.
20 S. J. Zhang, J. Hao, H. Wu, Q. Chen, C. Ye and S.-Z. Qiao, *Adv. Mater.*, 2024, **36**, 2404011.
21 J. Ma, M. Wang, H. Zhang, L. Fu, W. Zhang, B. Song, S. Lu, Q. Chen and K. Lu, *Mater. Today Energy*, 2022, **30**, 101146.
22 M. Xing, Z. Z. Zhao, Y. J. Zhang, J. W. Zhao, G. L. Cui and J. H. Dai, *Mater. Today Energy*, 2020, **18**, 100534.
23 B.-J. Lee, C. Zhao, J.-H. Yu, T.-H. Kang, H.-Y. Park, J. Kang, Y. Jung, X. Liu, T. Li, W. Xu, X.-B. Zuo, G.-L. Xu, K. Amine and J.-S. Yu, *Nat. Commun.*, 2022, **13**, 4629.
24 Y. Zhang, T. Zhao, S. Yang, Y. Zhang, Y. Ma and Z. Wang, *J. Energy Chem.*, 2022, **75**, 310–320.
25 H. Zhao, D. Yin, L. Zhao and S. Ding, *ChemNanoMat*, 2024, **10**, e202400004.
26 V. K. Thorsmølle, G. Rothenberger, D. Topgaard, J. C. Brauer, D.-B. Kuang, S. M. Zakeeruddin, B. Lindman, M. Grätzel and J.-E. Moser, *Chem. Phys. Chem.*, 2011, **12**, 145–149.
27 C. L. Bentley, A. M. Bond, A. F. Hollenkamp, P. J. Mahon and J. Zhang, *J. Phys. Chem. C*, 2015, **119**, 22392–22403.
28 X. Yang, H. Fan, F. Hu, S. Chen, K. Yan and L. Ma, *Nano-Micro Lett.*, 2023, **15**, 126.
29 F. Yang, J. Long, J. A. Yuwono, H. Fei, Y. Fan, P. Li, J. Zou, J. Hao, S. Liu, G. Liang, Y. Lyu, X. Zheng, S. Zhao, K. Davey and Z. Guo, *Energy Environ. Sci.*, 2023, **16**, 4630–4640.
30 Y. Tian, S. Chen, S. Ding, Q. Chen and J. Zhang, *Chem. Sci.*, 2023, **14**, 331–337.
31 J. Hao, L. Yuan, Y. Zhu, X. Bai, C. Ye, Y. Jiao and S. Qiao, *Angew. Chem., Int. Ed.*, 2023, **62**, e202310284.
32 Z. Gong, C. Song, C. Bai, X. Zhao, Z. Luo, G. Qi, X. Liu, C. Wang, Y. Duan and Z. Yuan, *Sci. China Mater.*, 2023, **66**, 556–566.
33 S. Wang, Y. Wang, Z. Wei, J. Zhu, Z. Chen, H. Hong, Q. Xiong, D. Zhang, S. Li, S. Wang, Y. Huang and C. Zhi, *Adv. Mater.*, 2024, **36**, 2401924.
34 Y. Liu, C. Lu, Y. Yang, W. Chen, F. Ye, H. Dong, Y. Wu, R. Ma and L. Hu, *Adv. Mater.*, 2024, **36**, 2312982.
35 J. Wu, J.-L. Yang, B. Zhang and H. J. Fan, *Adv. Energy Mater.*, 2024, **14**, 2302738.
36 F. Ye, R. Pang, C. Lu, Q. Liu, Y. Wu, R. Ma and L. Hu, *Angew. Chem.*, 2023, **135**, e202303480.
37 H. Kim, K. Kim, J. Ryu, S. Ki, D. Sohn, J. Chae and J. Chang, *ACS Appl. Mater. Interfaces*, 2022, **14**, 12168–12179.
38 K. Zhang, Q. Yu, J. Sun, Z. Tie and Z. Jin, *Adv. Mater.*, 2024, **36**, 2309838.
39 J. He, Y. Mu, B. Wu, F. Wu, R. Liao, H. Li, T. Zhao and L. Zeng, *Energy Environ. Sci.*, 2024, **17**, 323–331.
40 H. Xu, R. Zhang, D. Luo, J. Wang, K. Huang, J. Chi, H. Dou, X. Zhang and G. Sun, *Energy Storage Mater.*, 2023, **63**, 103019.
41 S. Wang, Y. Zhao, H. Lv, X. Hu, J. He, C. Zhi and H. Li, *Small*, 2023, **20**, 2207664.
42 Y. Lyu, J. Yuwono, P. Wang, Y. Wang, F. Yang, S. Liu, S. Zhang, B. Wang, K. Davey, J. Mao and Z. Guo, *Angew. Chem., Int. Ed.*, 2023, **62**, e202303011.
43 P. Lin, G. Chen, Y. Kang, M. Zhang, J. Yang, Z. Lv, Y. Yang and J. Zhao, *ACS Nano*, 2023, **17**, 15492–15503.
44 H. Xu, R. Zhang, D. Luo, J. Wang, H. Dou, X. Zhang and G. Sun, *ACS Nano*, 2023, **17**, 25291–25300.
45 W. Wu, C. Li, Z. Wang, H.-Y. Shi, Y. Song, X.-X. Liu and X. Sun, *Chem. Eng. J.*, 2022, **428**, 131283.
46 G. L. Bottger and A. L. Geddes, *Spectrochim. Acta*, 1965, **21**, 1701–1708.
47 R. Yao, L. Qian, Y. Sui, G. Zhao, R. Guo, S. Hu, P. Liu, H. Zhu, F. Wang, C. Zhi and C. Yang, *Adv. Energy Mater.*, 2022, **12**, 2102780.
48 Y. Zhang, S. Bi, Z. Niu, W. Zhou and S. Xie, *Energy Mater.*, 2022, **2**, 200012.
49 A. Bayaguud, X. Luo, Y. Fu and C. Zhu, *ACS Energy Lett.*, 2020, **5**, 3012–3020.
50 C. Huang, X. Zhao, S. Liu, Y. Hao, Q. Tang, A. Hu, Z. Liu and X. Chen, *Adv. Mater.*, 2021, **33**, 2100445.
51 L. Miao, Z. Guo and L. Jiao, *Energy Mater.*, 2023, **3**, 300014.
52 W. Shi, Z. Song, W. Zhang, S. Lian, F. Huang, Q. An and Q. Li, *Energy Environ. Sci.*, 2024, **17**, 7372–7381.
53 K. Guan, W. Chen, Y. Yang, F. Ye, Y. Hong, J. Zhang, Q. Gu, Y. Wu and L. Hu, *Adv. Mater.*, 2024, **36**, 2405889.
54 M. Yan, N. Dong, X. Zhao, Y. Sun and H. Pan, *ACS Energy Lett.*, 2021, **6**, 3236–3243.
55 K. Zhou, Z. Li, X. Qiu, Z. Yu and Y. Wang, *Angew. Chem., Int. Ed.*, 2023, **62**, e202309594.
56 C. Ji, Y. Luo, G. Guo, X. Li, C. Sun, M. Li, S. Yang, H. Mi and L. Sun, *Energy Storage Mater.*, 2024, **71**, 103615.
57 Z. Zhang, W. Ling, N. Ma, J. Wang, X. Chen, J. Fan, M. Yu and Y. Huang, *Adv. Funct. Mater.*, 2024, **34**, 2310294.
58 K. Wang, H. Li, Z. Xu, Y. Liu, M. Ge, H. Wang, H. Zhang, Y. Lu, J. Liu, Y. Zhang, Y. Tang and S. Chen, *Adv. Energy Mater.*, 2024, **14**, 2304110.
59 Z. Chen, F. Wang, R. Ma, W. Jiao, D. Li, A. Du, Z. Yan, T. Yin, X. Yin, Q. Li, X. Zhang, N. Yang, Z. Zhou, Q.-H. Yang and C. Yang, *ACS Energy Lett.*, 2024, **9**, 2858–2866.
60 W. Li, H. Xu, H. Zhang, F. Wei, T. Zhang, Y. Wu, L. Huang, J. Fu, C. Jing, J. Cheng and S. Liu, *Energy Environ. Sci.*, 2023, **16**, 4502–4510.
61 Q. Chen, S. Chen, J. Ma, S. Ding and J. Zhang, *Nano Energy*, 2023, **117**, 108897.
62 M. Liu, Q. Chen, X. Cao, D. Tan, J. Ma and J. Zhang, *J. Am. Chem. Soc.*, 2022, **144**, 21683–21691.

